NAVAL POSTGRADUATE SCHOOL

MONTEREY, CALIFORNIA

THESIS

WAKE DETECTION USING CONVOLUTIONAL NEURAL NETWORKS

by

Jacqueline Zimny

December 2021

Thesis Advisor: Timour Radko
Second Reader: Justin M. Brown

THIS PAGE INTENTIONALLY LEFT BLANK

REPORT DOCUMENTATION PAGE			Form Approved OMB No. 0704-0188

1. AGENCY USE ONLY *(Leave blank)*	2. REPORT DATE December 2021	3. REPORT TYPE AND DATES COVERED Master's thesis

4. TITLE AND SUBTITLE WAKE DETECTION USING CONVOLUTIONAL NEURAL NETWORKS	5. FUNDING NUMBERS RQQ2Q
6. AUTHOR(S) Jacqueline Zimny	
7. PERFORMING ORGANIZATION NAME(S) AND ADDRESS(ES) Naval Postgraduate School Monterey, CA 93943-5000	8. PERFORMING ORGANIZATION REPORT NUMBER
9. SPONSORING / MONITORING AGENCY NAME(S) AND ADDRESS(ES) Office of Naval Research, 875 North Randolph Street, Arlington, VA 22203	10. SPONSORING / MONITORING AGENCY REPORT NUMBER

11. SUPPLEMENTARY NOTES The views expressed in this thesis are those of the author and do not reflect the official policy or position of the Department of Defense or the U.S. Government.

12a. DISTRIBUTION / AVAILABILITY STATEMENT Approved for public release. Distribution is unlimited.	12b. DISTRIBUTION CODE A

13. ABSTRACT (maximum 200 words)

Advances in engineering and technology have made acoustic detection of submarines increasingly difficult. Using hydrodynamic signatures created by propagating submarines is an alternative method for submarine detection. Detection based on hydrodynamic signatures may also offer unique tactical advantages, given the tendency of wakes to persist for long timescales. Artificial neural networks trained on velocity field data show promise to automate detection. We used numerical simulations to generate velocity data on wake, jet, and convective turbulence. All these forms of turbulence have similar characteristics in the velocity field, yet their spectra reveal subtle differences that could be exploited for wake identification purposes. We then trained a convolutional neural network with the simulation results and demonstrated that neural networks can classify turbulent flows based on small-scale features with high accuracy. In particular, we find that the developed algorithms can successfully identify wakes in 92% of cases, which implies that the AI-based technology is viable and ready for the transition to the analysis of the experimental and field data.

14. SUBJECT TERMS wake, detection, artificial intelligence, neural networks, convection, jets, turbulence	15. NUMBER OF PAGES 57
	16. PRICE CODE

17. SECURITY CLASSIFICATION OF REPORT	18. SECURITY CLASSIFICATION OF THIS PAGE	19. SECURITY CLASSIFICATION OF ABSTRACT	20. LIMITATION OF ABSTRACT
Unclassified	Unclassified	Unclassified	UU

NSN 7540-01-280-5500

Standard Form 298 (Rev. 2-89)
Prescribed by ANSI Std. 239-18

THIS PAGE INTENTIONALLY LEFT BLANK

Approved for public release. Distribution is unlimited.

WAKE DETECTION USING CONVOLUTIONAL NEURAL NETWORKS

Jacqueline Zimny
Lieutenant Commander, United States Navy
BS, Texas A & M University, 2012

Submitted in partial fulfillment of the
requirements for the degree of

MASTER OF SCIENCE IN METEOROLOGY AND PHYSICAL OCEANOGRAPHY

from the

NAVAL POSTGRADUATE SCHOOL
December 2021

Approved by: Timour Radko
Advisor

Justin M. Brown
Second Reader

Peter C. Chu
Chair, Department of Oceanography

THIS PAGE INTENTIONALLY LEFT BLANK

ABSTRACT

Advances in engineering and technology have made acoustic detection of submarines increasingly difficult. Using hydrodynamic signatures created by propagating submarines is an alternative method for submarine detection. Detection based on hydrodynamic signatures may also offer unique tactical advantages, given the tendency of wakes to persist for long timescales. Artificial neural networks trained on velocity field data show promise to automate detection. We used numerical simulations to generate velocity data on wake, jet, and convective turbulence. All these forms of turbulence have similar characteristics in the velocity field, yet their spectra reveal subtle differences that could be exploited for wake identification purposes. We then trained a convolutional neural network with the simulation results and demonstrated that neural networks can classify turbulent flows based on small-scale features with high accuracy. In particular, we find that the developed algorithms can successfully identify wakes in 92% of cases, which implies that the AI-based technology is viable and ready for the transition to the analysis of the experimental and field data.

THIS PAGE INTENTIONALLY LEFT BLANK

TABLE OF CONTENTS

THIS PAGE INTENTIONALLY LEFT BLANK

LIST OF FIGURES

LIST OF TABLES

THIS PAGE INTENTIONALLY LEFT BLANK

LIST OF ACRONYMS AND ABBREVIATIONS

AI	artificial intelligence
CNN	convolutional neural network
DNS	direct numerical simulations
IVS	intense vorticity structures
LVS	large vorticity structures
MITgcm	Massachusetts Institute of Technology general circulation model
reLU	rectified linear unit
TNTI	Turbulent-Nonturbulent Interface

THIS PAGE INTENTIONALLY LEFT BLANK

ACKNOWLEDGMENTS

I would like to give thanks to my thesis advisor, Dr. Timour Radko, for allowing me latitude to learn and grow throughout this project. His enthusiasm and courage to explore a new field of artificial intelligence provided inspiration to complete this project.

Many thanks to Dr. Justin Brown, who made this project possible. His patience and guidance were instrumental throughout data collection and model training. I very much appreciate his dedication to students and being available to answer my endless questions. Without him, I would not have gained confidence using high performance computing.

I would like to thank the rest of the Meteorology and Oceanography departments, who have provided me with the necessary skills to think critically and solve problems.

I am forever grateful for learning a great deal from my peers, Austin, Josh, Scott, Brandon, Shelly, Allison, Mike B, Mike A, Meredith, Chris, Alex, and Matt.

I would like to acknowledge the Department of Defense (DOD) High Performance Computing Modernization Program Onyx for running efficiently to produce data from the Massachusetts Institute of Technology general circulation model (MITgcm).

Most importantly, I would like to give thanks to my husband, Thomas, who supported me and our children, Natalia and Erik, throughout my time at the Naval Postgraduate School.

THIS PAGE INTENTIONALLY LEFT BLANK

I. INTRODUCTION

A. MOTIVATION

Sonar detection of submarines has become increasingly challenging in recent years due to advances in noise-reducing technology such as air-independent propulsion systems, noise-reducing tiles, and improved propeller screw design. The detection of hydrodynamic signatures produced by submarines may serve as a promising alternative to traditional means of submarine detection. It is well documented that aquatic organisms can detect hydrodynamic signals generated by moving submerged objects (Dehnhardt et al., 2001). This suggests that different flow patterns could be identified from local conditions alone. It is unclear what hydrodynamic features can distinguish submerged objects from environmental turbulent features. However, it may be possible to identify these features using the recently developed deep machine learning algorithms with image and pattern recognition capabilities. Such AI-based models, trained on the numerically generated or experimental data, would enhance submarine detection capabilities.

B. BACKGROUND

1. Relevant Dimensionless Parameters

In studies of turbulent wakes, several non-dimensional parameters provide a means for quantifying the relative significance of various physical processes. For example, the Reynolds Number (Re) measures the relative contribution of advective and dissipative processes, as described in the following equation:

$$\mathrm{Re} = \frac{UL}{\nu}, \tag{1}$$

where U is the velocity of the body, L is the length scale, and ν is the viscosity of the fluid. The Reynolds number determines the initial intensity of turbulence generated after the passage of a propagating object. For very small values of Re, viscous forces dominate, the flow is laminar, and the transfer of momentum occurs on molecular scales. Vortex shredding can occur at larger Reynolds numbers between 500 and 2000. At a critical value of Re, usually around 4000, the fluid becomes turbulent and disorganized, and the primary

mechanism of momentum transport is by turbulent structures. The turbulent structures contain kinetic energy which cascades from the largest turbulent structures to smaller structures and continues until viscous forces dissipate the energy into heat at the viscous scale.

The Froude number (Fr) describes the relative strength of inertial and buoyancy forces, as described by the following equation:

$$\mathrm{Fr} = \frac{U}{NL}, \tag{2}$$

where the Brunt-Väisälä frequency, N, is defined as:

$$N = \sqrt{-\frac{g}{\rho}\frac{d\rho}{dz}}, \tag{3}$$

where g is the gravitational acceleration, and ρ is the density of the fluid. When the Froude number is less than unity, buoyancy forces dominate the flow, and the wake is flattened by the stratification of the system. Chomaz et al. (1993) demonstrated the effects of the Froude number through a series of laboratory experiments. They showed that the typical wake structure has a larger vertical extent at larger Froude numbers until the Froude number reaches a critical value of one. Above this value, the flow is dominated by lee waves until the Froude number increases to 1.5, where turbulent wake structures reappear. These structures are initially uninfluenced by stratification until the time since passage exceeds a buoyancy period at which point the wake will begin to flatten as before. Once the Froude number surpasses 4.5, Chomaz et al. (1993) found that this initial turbulent flow resembles a turbulent flow in the homogenous fluid.

2. Wake Turbulence

The turbulent vortices produced by a propagating submerged object are well studied in numerical simulations (see Gourlay et al., 2001; Dommermuth et al., 2002; Diamessis et al., 2005; Diamessis et al., 2011; Chongsiripinyo et al., 2017) and laboratory experiments (see Afanasyev, 2004; Bonneton et al., 1993; Chomaz et al., 1993; Lin et al., 1992; Meunier & Spedding, 2006; Spedding, 1997; Spedding et al., 1996a,b). In particular, Spedding (1997) demonstrated that the wake of a propagating object undergoes three stages: the near

wake, the non-equilibrium (NEQ) regime, and the quasi-two-dimensional wake. The near wake appears as a flow with isotropic turbulence that expands horizontally and vertically. As the turbulence decays, the flow transitions to the NEQ regime, which is characterized by the increasing influence of buoyant forces compressing the isotropic turbulent structures. This phenomenon was observed in fluids with initial Froude numbers ranging from 1 to 240 (Spedding 1997), indicating that transitioning to the NEQ regime occurs even when the initial Froude number is high. Eventually, vertical motions are minimized in the far wake, and the previously isotropic structures are suppressed into a quasi-two-dimensional state where pancake vortices are observed (Spedding 1997).

Turbulent wake structures created from propagating submerged bodies behave similarly and quickly display some degree of organization. Early wake structures are dependent on the shape of the propagating body initially but lose the memory of the geometry of the propagating body over time (Meunier and Spedding 2004). The structure of vortices shedding from the propagating body is sensitive to the Reynolds number. As the Reynolds number approaches infinity, the radii of the vortical core systematically decrease, while their vorticities increase unbounded. Then many of these vortices undergo a spin-down, an increase in radii, and may interact or merge with other vortices (Lewis and Radko 2020). As the wake decays, the coherent structures of the isotropic turbulence persist while small-scale vorticity fluctuations dissipate (Spedding 2014). It may be possible to distinguish these persistent structures from environmental turbulence by studying the flow patterns, but this requires expertise. We can compare turbulent wake structures with those created from other sources of ambient turbulence in the ocean to uncover unique characteristics of turbulent wakes that could be used for detection.

3. Other Sources of Turbulence

Ambient ocean turbulence can be generated by a variety of processes, either internally or through interactions with the ocean boundaries. Internally generated turbulence could potentially be generated by a shear flow from a jet or an internal wave. Turbulence generated at the boundaries would include processes such as tidal flows over the sea-floor, convection resulting from cooling at the surface boundary, geothermal

heating, or wind-induced turbulence near the surface. The author recommends Thorpe (2007) for a general overview of oceanic turbulence. To compare wake turbulence with turbulence generated from other sources, we consider turbulent flow generated from jets and wave breaking as examples.

a. Jets

Many numerical simulations examining turbulent stratified wakes are initialized with a jet, by prescribing a mean velocity profile and small perturbations. However, differences between turbulent jet flows and stratified wakes can be substantial. The systematic dissimilarities of structures that emerge in late evolutionary stages could be used to distinguish between turbulent jet and stratified wake flows. Analysis of the numerical simulations shows that jet and late wake flows are generally consistent in terms of the temporal evolution of the length and velocity scales. Turbulent wakes, however, are affected by a solid boundary of an object that could form a viscous boundary layer, permitting the development of small-scale features initially. In jets, eddies are determined at jet scales and then cascade into smaller scales over time. Since the small structures in the wake dissipate due to stratification, it follows that a turbulent jet would resemble a stratified late wake. This reasoning supports the approximation of the late wake with a numerically simulated jet demonstrated by Radko and Lorfeld (2018). Any differences between stratified wakes and jets uncovered in this study should be examined and considered before drawing conclusions about stratified wakes based on simulated jet flows.

Nonlinear interactions and dynamic instabilities amplify perturbations in the mean velocity of jets, developing into turbulence. The surrounding fluid becomes entrained into the turbulent flow. Turbulent structures generated from jets produce Intense Vortical Structures (IVSs) and Large Vortical Structures (LVSs). IVSs are structures with particularly high vorticity, defined as vortical structures with the highest 1% vorticity of the flow (Jiménez et al. 1993). LVSs are the largest vortical structures in the flow. The radius, length scales, and lifetime of LVSs are related to the instabilities that generated them, however they generally have a tubular shape and are governed by inviscid laws. The

LVSs define the outer edge of the jet, known as the Turbulent-Nonturbulent Interface (TNTI), which is a thin region that separates turbulent flow from the irrotational fluid.

b. Internal Wave Breaking

Internal waves can induce convective or shear turbulence following the breaking of an internal wave, where strong oscillations of density in the water column can lead to instability. Dense water can be displaced over light water until the wave breaks and the flow becomes turbulent. Because internal waves are generated by tides, the available turbulent features have frequencies between the inertial frequency and the Brunt-Väisälä frequency. Garrett and Munk (1972, 1975, 1981) provided a detailed model for the dissipation of energy in this inertial range. More recently, numerical simulations have offered an opportunity to explore the characteristics of the turbulent patches generated from internal waves. For example, Yakovenko et al. (2011) showed that these turbulent structures can persist for long periods and are not dissimilar from late wakes. To develop a means to distinguish between persistent turbulent structures such as these and a wake, we turn to artificial neural networks.

4. Machine Learning Applications to Turbulence Identification

Despite the wide applicability of machine learning to pattern recognition, there have only been a few attempts to apply Artificial Neural Networks (ANN) to turbulence. Early applications for object detection in natural images included face detection and localization in images (Vaillant et al. 1994) and facial recognition (Lawrence et al. 1997). The image recognition has since been expanded to turbulence modeling; Zhang and Duraisamy (2015) used a standard feed-forward neural network to model the functional terms in Reynolds Averaged Navier-Stokes calculations, finding that the spatial functional correction term to RANS and was well represented by the neural network. This demonstrated that machine learning can be a valuable tool for analyzing turbulent flows. Moreover, ANN has also been used to distinguish between turbulent flows of an oscillating air flow by feeding time-series data of the vorticity field into a network (Colvert et al. 2018). The network was able to classify the wake type generated by the oscillating air flow from local measurements alone with at least 90% accuracy.

Given the similarities between LVSs of various turbulent flows and the lack of memory in vortical structures in the intermediate and late wakes, detection of a wake from local measurements is difficult. This study has found that convolutional neural networks are able to distinguish unique characteristics of a wake's velocity field from environmental turbulence. Chapter II will describe the numerical simulation methodology used to create data samples for the wake and environmental turbulence. Chapter III will discuss the results of the numerical simulations. Chapter IV will detail the convolutional neural network used in this study. Chapter V will provide the results of the training and validation of the neural network. Chapter VI will offer a discussion and conclusion of the results.

II. NUMERICAL SIMULATIONS METHODOLOGY

We employ the Massachusetts Institute of Technology General Circulation Model (MITgcm), which is a flexible computational fluid dynamics solver that can simulate oceanographic phenomena from basin-wide scales to micro-scales (Marshall et al. 1997). MITgcm uses a finite-volume method and can be configured to solve the equations of motion using the Boussinesq approximation. These equations of motion are given by

$$\nabla \cdot \mathbf{u} = 0, \tag{4}$$

$$\frac{\rho - \rho_0}{\rho_0} = -\alpha(T - T_0), \tag{5}$$

$$\frac{\partial T}{\partial t} + \mathbf{u} \cdot \nabla T = k_\mathrm{T} \nabla^2 T + Q, \tag{6}$$

$$\frac{\partial \mathbf{u}}{\partial \mathrm{t}} + \mathbf{u} \cdot \nabla \mathbf{u} = -\frac{1}{\rho_0} \nabla p - \frac{\rho}{\rho_0} g \hat{\mathbf{k}} + \nu \nabla^2 \mathbf{u} + F \hat{\mathbf{i}}, \tag{7}$$

where $\mathbf{u}$ is the velocity vector, ρ is density, ρ_0 is a reference density, α is the thermal expansion coefficient, T is temperature, k_T is the thermal diffusivity, $\hat{\mathbf{k}}$ is the unit vector in the z-direction, $\hat{\mathbf{i}}$ is the unit vector in the x-direction, and ν is the kinematic viscosity. Equation 4 describes mass continuity, Equation 5 is the linear equation of state, Equation 6 describes the temperature evolution, and Equation 7 is the momentum evolution equation. The Q and F terms are external heating and forcing functions, respectively, which are used to generate turbulence.

a)

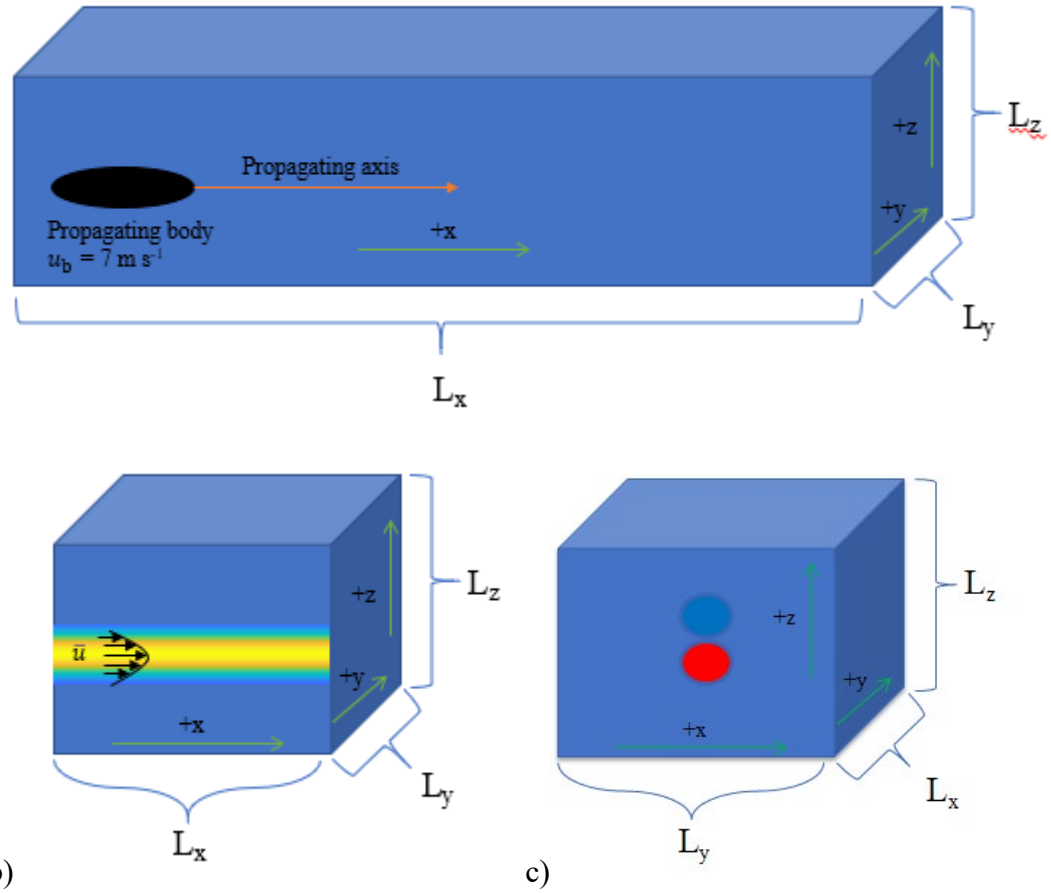

b) c)

Figure 1. The simulation domain, where L_x is the length of the domain in the x direction, L_y is the length of the domain in the y direction, and L_z is the length in the z direction. The green arrows demonstrate the positive direction for x, y, and z. Panel a) depicts the simulated wake, panel b) depicts the simulated jet, and panel c) depicts the convection simulation.

Table 1. Domain parameters

	Wake	**Jet**	**Convection**
Parameter	Value	Value	Value
Viscosity ($\boldsymbol{\nu}$)	$4.5 \times 10^{-3}\mathrm{m^2s^{-1}}$	$8.0 \times 10^{-3}\mathrm{m^2s^{-1}}$	$1.0 \times 10^{-1}\mathrm{m^2s^{-1}}$
Thermal diffusivity ($\boldsymbol{k_T}$)	$4.5 \times 10^{-3}\mathrm{m^2s^{-1}}$	$8.0 \times 10^{-3}\mathrm{m^2s^{-1}}$	$1.0 \times 10^{-1}\mathrm{m^2s^{-1}}$
Thermal expansion coefficient ($\boldsymbol{\alpha}$)	$2.0 \times 10^{-4}\mathrm{°C^{-1}}$	$2.0 \times 10^{-4}\mathrm{°C^{-1}}$	$2.0 \times 10^{-4}\mathrm{°C^{-1}}$
Domain length in x ($\boldsymbol{L_x}$)	938.7m	117m	117m
Domain length in y ($\boldsymbol{L_y}$)	100m	100m	100m
Domain length in z ($\boldsymbol{L_z}$)	100m	100m	100m
$\boldsymbol{A_u}$	-	1 m/s	-
$\boldsymbol{A_c}$	-	-	7m°C
σ	5m	5m	5m

Each simulation is run in a three-dimensional domain in x, y, and z with a background temperature gradient of $0.03°\mathrm{Cm}^{-1}$ and with small perturbations taken from a uniform distribution. All simulations have 0.33 m resolution in all spatial directions. Figure 1 depicts the simulated domain for all cases. We define L_x, L_y, and L_z as the lengths of the domain in the x, y, and z directions, respectively. The domain sizes for each simulation are included in Table 1, which fully describes the characteristic parameters of each simulation.

A. PROPAGATING OBJECT

To study the turbulence of a wake, an ellipsoid is towed through a quiescent medium at a velocity u_b along its longest axis. The forcing F is defined as

$$F = \begin{cases} \frac{u-u_\mathrm{b}}{\tau}, \text{inside object,} \\ 0, \text{ elsewhere,} \end{cases} \tag{8}$$

where τ is the relaxation time over which the body velocity is 7ms^{-1}. The propagating object has an ellipsoidal geometry, bounded by

$$1 < \frac{(x-x_\mathrm{b})^2}{{\sigma_\mathrm{x}}^2} + \frac{(y-y_\mathrm{b})^2}{\sigma^2} + \frac{(z-z_\mathrm{b})^2}{\sigma^2}, \tag{9}$$

where x_b, y_b, and z_b describe the position of the propagating body, σ is the length of the principle semi-axes in *y* and *z*, and σ_x is the principle semi-axis in *x*. Additionally, we implemented an immersed boundary condition at the surface of the ellipsoid. We assign σ as 5m, and σ_x as 50m for naval relevance. The position of the propagating ellipsoid in the *x* coordinate is given by

$$x_\mathrm{b} = u_\mathrm{b} t + x_{0,\mathrm{b}}, \tag{10}$$

where $x_{0,\mathrm{b}}$ is the starting point in x, which is 100m away from the -*x* boundary. The origin of the domain is set to be the surface point at the -*x*, -*y* vertex. The position of the body in *y*, y_b, is 100m, and the position in *z*, z_b, is -50m.

B. JET

To generate a form of turbulence to contrast with the wake, we consider the turbulence generated by a continuously forced jet. We simulate a jet flow by creating an initial velocity profile defined as

$$\bar{u} = A_\mathrm{u} e^{\frac{-(y-y_0)^2-(z-z_0)^2}{\sigma^2}}, \tag{13}$$

where $\bar{u}$ is the bulk velocity in the *x*-direction, A_u is the amplitude of the jet (1m/s) at the jet axis center, and σ describes the characteristic radius of the jet, which we placed at $y_0 = 50\mathrm{m}$ and $z_0 = -50\mathrm{m}$. The jet amplitude is perturbed by a small sinusoid along the *x* direction to seed instability. We continuously force the jet and allow perturbations to evolve into turbulence over time. The forcing for the jet, *F*, is given by

$$F = \frac{\gamma_u}{\tau}\bar{u}, \tag{14}$$

where γ_u is defined as

$$\gamma_u = -\frac{\int(u-\bar{u})\bar{u}dV}{\int \bar{u}^2 dV}, \tag{15}$$

which allows us to adjust the mean velocity without affecting the microstructures that are valuable to this study.

C. CONVECTION

As our second example of non-wake turbulence, we continuously generate convective motions by localized heating and cooling. To produce convective turbulence, we forced a dipole in the temperature field, with a region of persistent cooling directly above a region of persistent heating. This forcing generates local instability, driving vertical motions and turbulent flow. Persistent thermal forcing, Q, was introduced to induce convection and is defined as follows:

$$Q = \frac{\gamma_c}{\tau}\bar{T}, \tag{16}$$

where γ_c is given by

$$\gamma_c = -\frac{\int(T'-\bar{T})\bar{T}dV}{\int \bar{T}^2 dV}, \tag{17}$$

and $\bar{T}$ is the desired temperature dipole, described by

$$\bar{T} = -\frac{2A_c}{\sigma^2}(z-z_0)e^{\frac{-(y-y_0)^2-(z-z_0)^2}{\sigma^2}}, \tag{18}$$

where A_c determines the amplitude of the convective forcing, and T' is the thermal perturbation away from the horizontally averaged temperature field ($\langle T \rangle$), given by

$$T' = T - \langle T \rangle. \tag{19}$$

Stratification-driven turbulence such as this likely carries different signatures than the wake and jet cases as forcing is largely vertical for convection and horizontal for wakes and jets.

III. SIMULATION RESULTS

Figure 2 displays the *x* component of the velocity field, *u*, of the simulation with an ellipsoid propagating at 7 m/s. At early times, the flow around the body is laminar prior to the onset of turbulence, which is evidenced by the structure of the wake at x < 200m. Soon thereafter, near wake turbulence forms behind the propagating ellipsoid (see Figure 2a) and remains in the domain throughout the simulation. The laminar feature near *x*=200m is a startup transient, and so we only use data after *x*=300m for analysis. The near wake structures have not yet experienced the effects of buoyancy forces and therefore have not yet transitioned to intermediate wake structures. We see that the smallest scale features created immediately after the passage of the body dissipate quickly, and the larger features persist and are generally the same size as each other. These characteristics uncovered from studying near wake turbulence will serve as a baseline for turbulent wake classification. We now consider the turbulent structures generated from environmental flows for comparison.

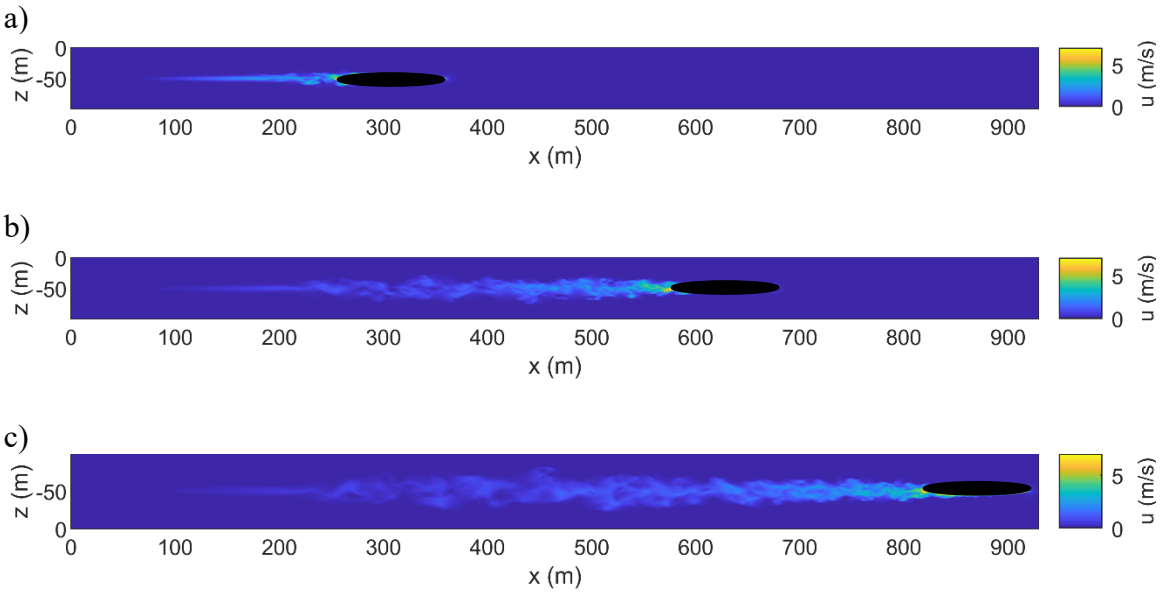

Figure 2. The *x* component of the velocity field at y = 100m, *u*, of the ellipsoid case with $u_b = 7$m/s after a) 30 seconds b) 75 seconds and c) 110 seconds.

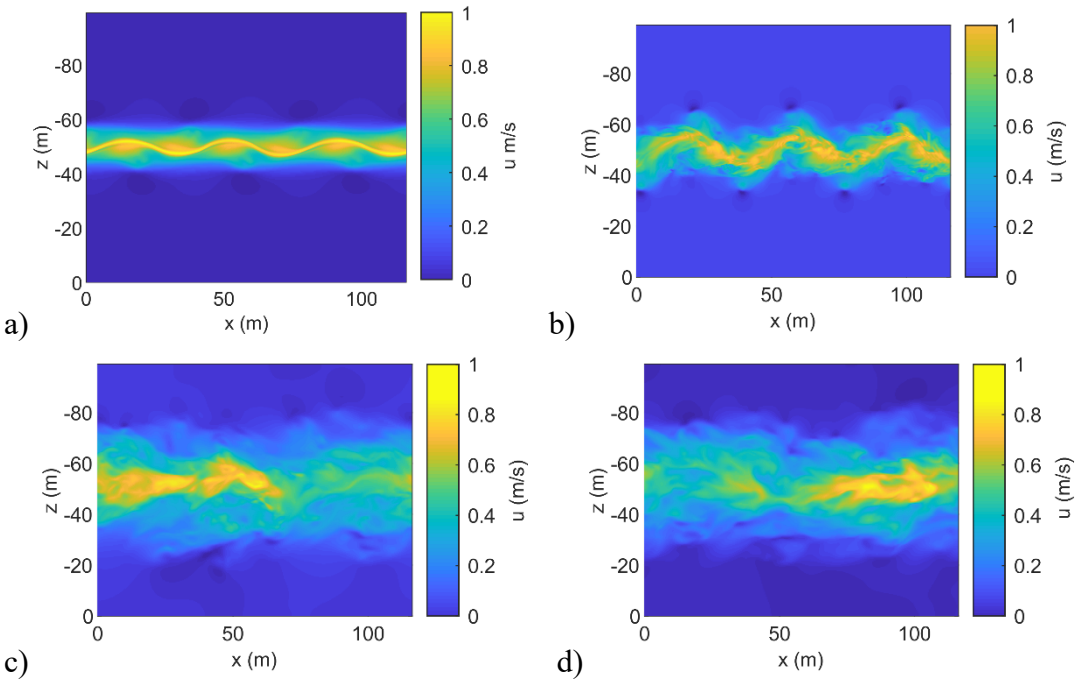

Figure 3. The *x* component of the velocity field, *u*, of a simulation with a continuously forced, 1 m/s jet. Panel a) shows a sinusoidal structure developing at 210 seconds. Panel b) shows the turbulent structures generated from instabilities in the sinusoidal displacements at 340 seconds. Panels c and d show the migration of the jet maximum in the positive x-direction at 1860 and 1990 seconds, respectively.

Figure 3 displays the production of turbulent flow from a continuously forced 1m/s jet. At the beginning of the simulation, the initial sinusoidal perturbations in the jet amplitude grow and large vortical structures form at the jet edges (see Figure 3a). Nonlinear interactions continue to influence the shape of the jet until the flow becomes turbulent (see Figure 3b). The early jet in Figures 3a and 3b is narrow, but it widens over time as fluid becomes entrained into the turbulent flow, which is evidenced by the broadened wakes in Figures 3c and 3d. The maximum extent of this turbulent flow is known as the Turbulent/Nonturbulent Interface (TNTI). The continuously forced jet continues to generate turbulent flow, with the most intense flow remaining in the vicinity of the jet axis. A jet maximum, a region of highest velocity, forms and migrates over time in the positive *x*-direction (see figures 3c and 3d). The presence of large vortical structures, the TNTI, and a jet maximum that migrates over time are defining features of the jet and could be used

for jet classification. This provides a useful comparison for turbulence generation of laterally driven flows.

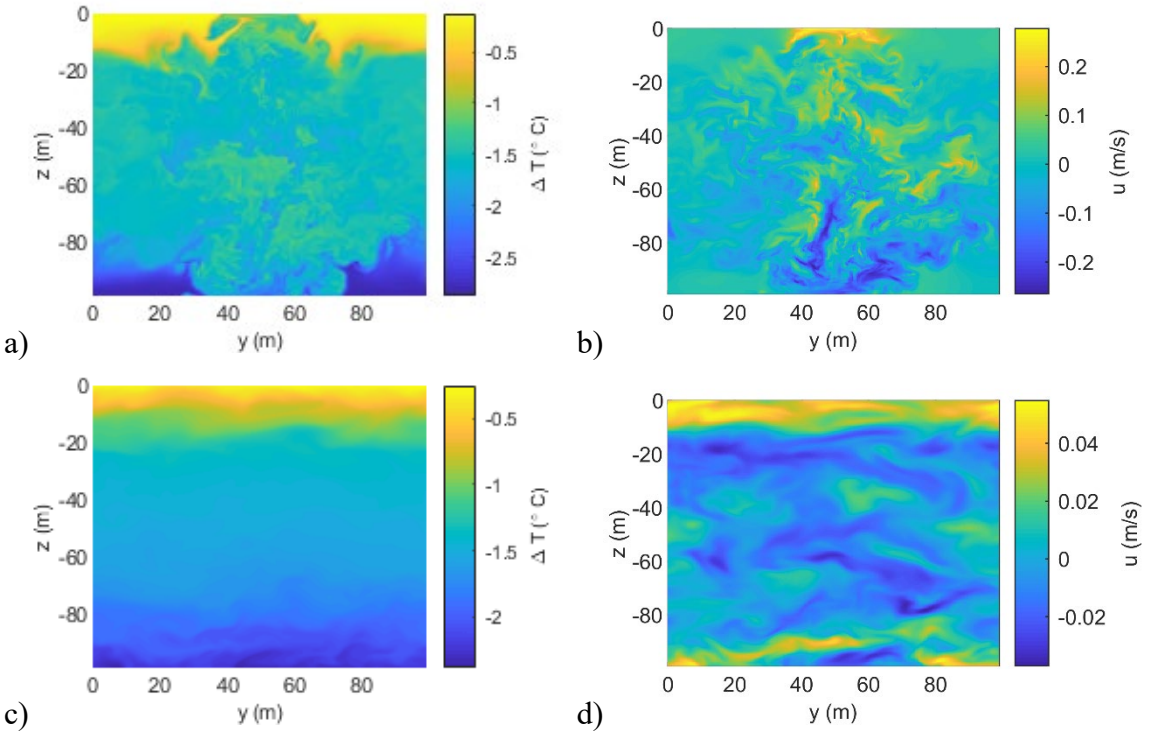

Figure 4. The temperature field and x component of the velocity field for the convection case at $t = 188.5$s and $t = 4470$. The temperature field is displayed in Figures a) and c), respectively. The x component of the velocity field, u, for the same times are shown in b) and d), respectively.

For vertically driven flows, we find that persistent forcing of convection also produces turbulent structures from a stratified fluid. The temperature field, shown as the difference of temperature from the surface temperature, ΔT, in Figure 4a shows fluid with fairly uniform temperature in the center, where plumes of warm and cool fluid have introduced mixing. There remains fluid that has not been mixed by convective turbulence near the upper and lower boundaries, which remains stratified. Away from this boundary layer, the turbulence fills the domain isotropically, which distinguishes it from wake or jet turbulence. The development of turbulence that is isotropic over large scales may be used to classify this source of turbulent mixing.

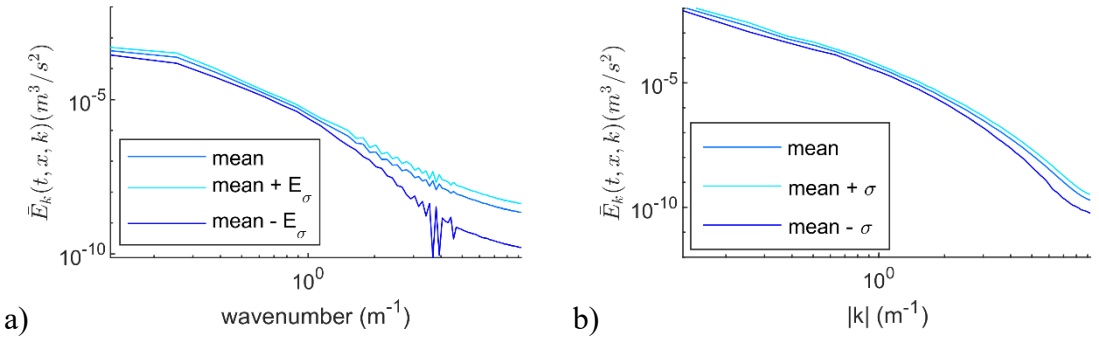

Figure 5. The panel a) depicts the energy density mean, mean plus one standard deviation, E_σ, and mean minus standard deviation for a jet. The panel b) depicts the energy density mean, mean plus one standard deviation, and mean minus standard deviation for convection.

Figure 5 shows the kinetic energy density spectra of environmental turbulent flows, which help to identify properties of turbulence that might help to classify these systems. To determine the kinetic energy density, we define the specific kinetic energy, K, as

$$K = \frac{1}{2}(u^2 + v^2 + w^2), \tag{20}$$

from which the kinetic energy density at position x and at time t is given by

$$E_k(t, x, k_y, k_z) = \mathcal{F}(K(t, x, y, z)), \tag{21}$$

where k_y and k_z are the y and z components of the wavevector, $\mathbf{k}$, and $\mathcal{F}$ is the two-dimensional discrete Fourier transform in y and z. We separate k into 50 discrete bins, where the ith bin has a wavenumber of $k_i = \frac{i\, k_{\max}}{50}$ for $k_{\max} = 9.4$. The mean kinetic energy in each bin, $\bar{E}_k(t, x, k_i)$, is the mean of $E_k(t, x, k_y, k_z)$ for all modes that meet the condition $k_i < \sqrt{{k_y}^2 + {k_z}^2} < k_{i+1}$. These two-dimensional spectra are calculated from slices taken normal to the x-axis at 33m intervals. We calculate the mean and standard deviation, E_σ, of the spectra from these slices, and then plotted the mean, mean plus standard deviation, and mean minus standard deviation to indicate the typical range of energies at any given wavenumber. The energy injection scale for both cases is at wavenumber 0.63m^{-1}, determined by the size scale of the forcing (2σ). In the inertial

range between the injection scale and the Kolmogorov length scale, energy cascades from the injection scale to higher wavenumbers where larger turbulent structures break into smaller structures until they reach the Kolmogorov length scale, whereafter viscous dissipation dominates. We assume the model can resolve features up to the Kolmogorov length scale. We also see energy at smaller wavenumbers than the injection scale, which indicates an inverse energy cascade.

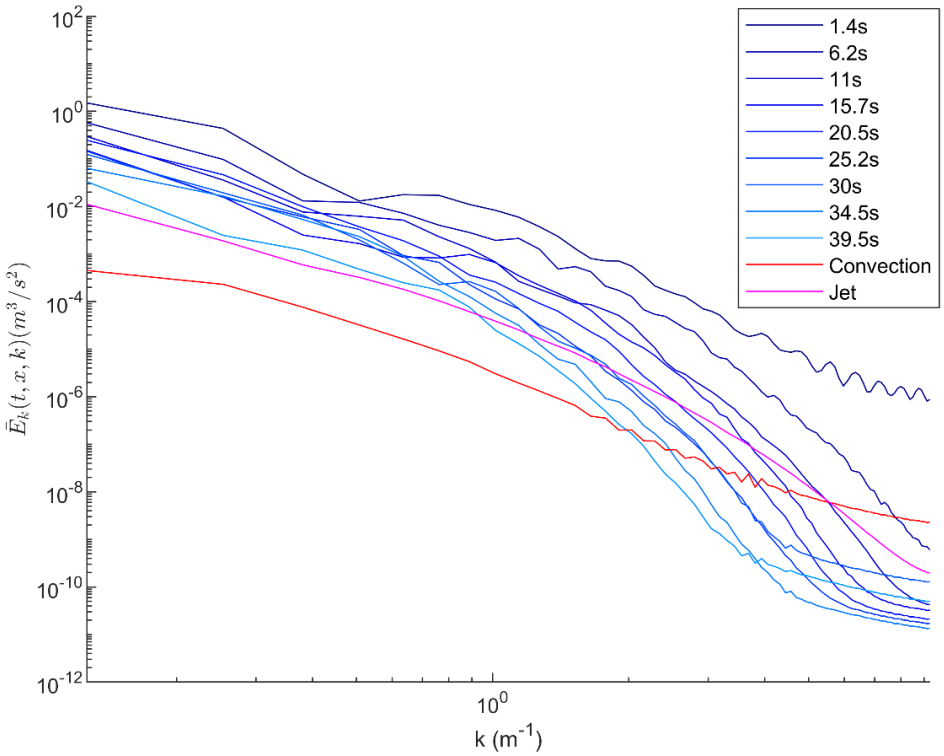

Figure 6. The energy density spectra of the wake case in blue at various times since the passage of the propagating ellipsoid (indicated in the legend), mean convection in a red line, and mean jet in a magenta line. The colors of the wake spectra become lighter as the time since object passage increases.

In Figure 6, we plot the spectra for varying times since the propagating body has passed, finding that as time elapses, the kinetic energy density decreases. These two-dimensional spectra are calculated from slices taken normal to the *x*-axis at 33m intervals

starting at x = 333m to ignore the startup transient feature. The general shape of the spectrum in the wake case shows a gradual decrease in slope to contrast the power law of convective turbulence. We also see variability in the energy density structure of the wake case. For example, a local minimum exists at wavenumber $0.5m^{-1}$ for the spectrum calculated at 6.2 seconds since the passage of the propagating body. Other spectra do not appear to have such a local minimum, such as the spectra calculated at 34.5 seconds since the passage of the propagating body. Since the inertial range of the spectra differs between the wake case and the environmental cases, especially at higher wavenumbers, an artificial neural network may distinguish wake turbulence from environmental turbulence based on small-scale features.

IV. ARTIFICIAL NEURAL NETWORK METHODOLOGY

Artificial neural networks process a series of inputs through a sequence of "layers," which analyze the data, identify persistent patterns, and produce a series of outputs. Each layer in the network takes its inputs and produces its own outputs using trainable parameters. These parameters are adjusted until the network yields the optimal results during a training phase. In a fully connected layer, the output of each layer consists of a set of nodes that are connected via a neuron to each node in a previous layer, which has an input value **s**. The layer will multiply **s** by a weight matrix (**W**) and add a bias vector, **b**, to create a new set of values, **q**. This process can be represented by the following expression:

$$q_{ij} = W_{ij}s_{ij} + b_j. \tag{22}$$

The resulting values are then fed through an activation function to normalize or otherwise constrain the results. In our case, this activation function is the rectified linear unit (ReLU), where any input less than zero is set to zero, such that

$$\mathrm{ReLU}(q_{ij}) = \begin{cases} 0, & q_{ij} < 0, \\ q_{ij}, & q_{ij} \geq 0. \end{cases} \tag{23}$$

The process continues in each layer, and the last layer provides the classification determination. The activation function in the final layer is the "softmax" function which is given by

$$c_i = \mathrm{softmax}(q_i) = \frac{\exp(q_i)}{\sum_{j=1}^{k} \exp\,(q_j)} \tag{24}$$

The sum of these outputs layer is unity, so the final result of the classification layer, c_i, is the probability that the input belongs to class *i*. During the training phase, c_i equals one if the image belongs to class *i* and zero otherwise. While the system is training on the input data, the algorithm will adjust values of **W** and **b** in each layer to minimize error. In a supervised approach, the results of the predicted output of the algorithm are compared to a known output that the user creates. Large input data sets, such as pixels in a group of images, require more layers to simplify complex patterns (Theobald, 2017). After the training phase, the network goes through validation to determine the accuracy of the model.

Separate input and output data are reserved for the validation phase, and not used during the training phase.

During the training phase, the algorithm minimizes the loss of the network, defined using a cross-entropy function:

$$\text{loss} = -\frac{1}{S}\sum_{l=1}^{S}\sum_{i=1}^{K} w_i t_{il} \ln c_{il} \tag{25}$$

in the classification layer, where S is the number of samples, K is the number of mutually exclusive classes, w_i is the weight for class j (unity in this study), t_{il} is unity if sample l is a member of class i and zero otherwise, and c_{il} is the output of the softmax layer for sample l. The algorithm determines the weights and biases of the network to minimize the loss of incorrectly classified samples using stochastic gradient descent with a momentum optimizer. After the training phase, the network is used for classifying the reserved validation data set. The accuracy of the network classification is determined by taking the sum of correctly classified data divided by the total number of samples in the validation set.

A. CONVOLUTIONAL NEURAL NETWORKS

ANNs that employ convolution for mathematical analysis are called convolutional neural networks (CNN). Convolution is useful for the application of machine learning to image datasets because the same convolution filter is applied at every position in the input. This permits the network to identify common features with lower storage requirements than traditional neural networks. This is due to the convolution being equivariant to translation. This property of convolution is valuable to analyze a feature in an image that moves through time, for example (Goodfellow et al. 2016). We employ the use of a convolutional neural network to identify unique turbulent structures between those created by a propagating ellipsoid, a jet, and convection. The MATLAB Deep Learning Toolbox (The MathWorks, Inc 2018) is used to define the neural network architecture, train and validate the network, and compute the accuracy of the model.

After the convolutional layer, a batch normalization layer is typically used to normalize the results prior to the rectified linear unit activation function. The batch

normalization layer normalizes a small batch of data for all observations for each channel independently by subtracting the mean of a batch and dividing the results by the batch standard deviation. This provides the algorithm with an offset **β** and scale factor **μ**, which are learnable parameters that update during network training. The key feature of the batch normalization layer is that it normalizes the activations and gradients propagating through the network, making the classification optimization problem easier.

B. DATASET PREPARATION

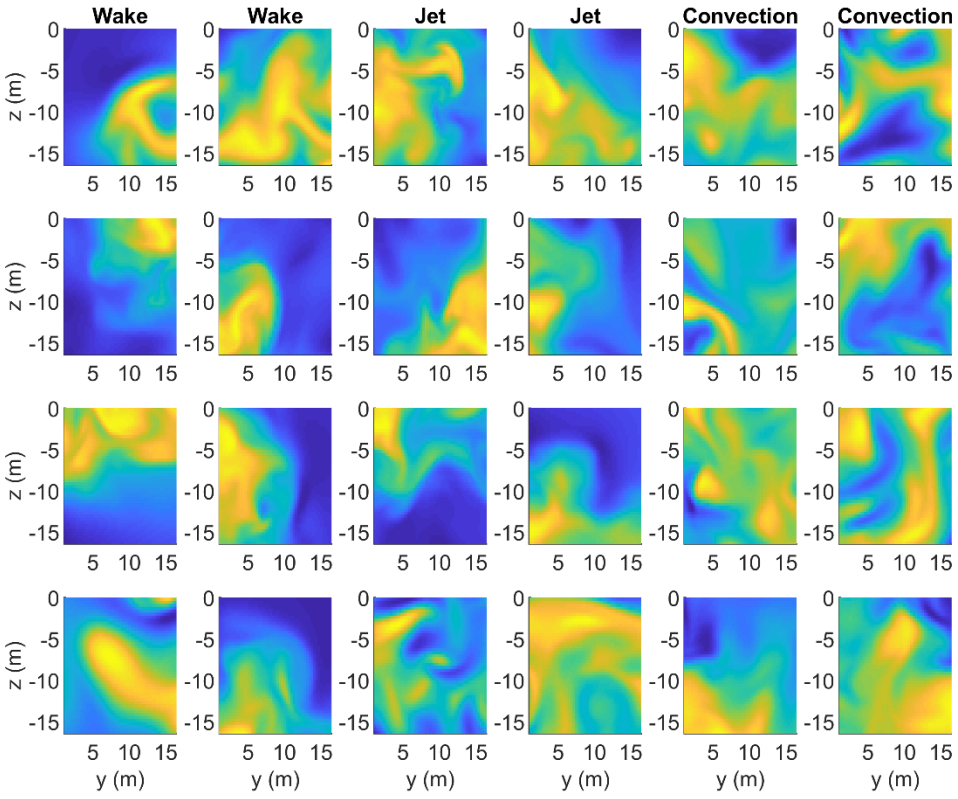

Figure 7. Samples for each case of the normalized *x* component of the velocity field. The first two columns show wake samples, the 3rd and 4th columns show jet samples, and the 5th and 6th columns show convection samples.

The inputs to the convolutional neural network are taken from slices of the simulations presented in Chapter III. The temperature and all components of the velocity

field are gathered at varying times and slice displacements specific to the individual case. We base the slice displacements on the intervals at which samples are decorrelated, approximately every 500m, 25m, and 200m for the wake, jet, and convection cases, respectively. The samples are then broken up into 17m-by-17m segments and then normalized by dividing each point by the root mean square (rms) of the sample. Figure 7 shows two-dimensional samples of u as they would be used in the input layer of the network for each case. Some samples have features that encompass a large portion of the image, whereas some samples only have small features and others have both, which tells us that the samples provided the network with a variety of different length scales for analysis.

C. NETWORK ARCHITECTURE

The network has five types of layers: the input layer, the convolutional layers, the pooling layers, the fully connected layer, and the classification layer. The input layer takes a two dimensional sample of the u velocity field generated by the simulation. The data then go through each convolutional layer. If the input to a convolution layer is N_x by N_z, contains n channels, and the layer has m feature maps each of size N_x by N_z by n, the resulting output is N_x by N_z by m. Each subsequent channel represents the result of the convolution of the input with the associated feature map. To reduce computational load, we apply a pooling layer which reduces the complexity of the classification problem by separating the physical dimensions of the convolution results into rectangular pools and taking the maximum of the convolution results in that pool. The results of the third layer are sent to the fully connected layer, which connects each input to a potential classification. The activation function for the convolution layers is the rectified linear unit function. As the fully connected layer is the final layer in the system, the activation function is the soft max function. This yields the final probabilities for the classification.

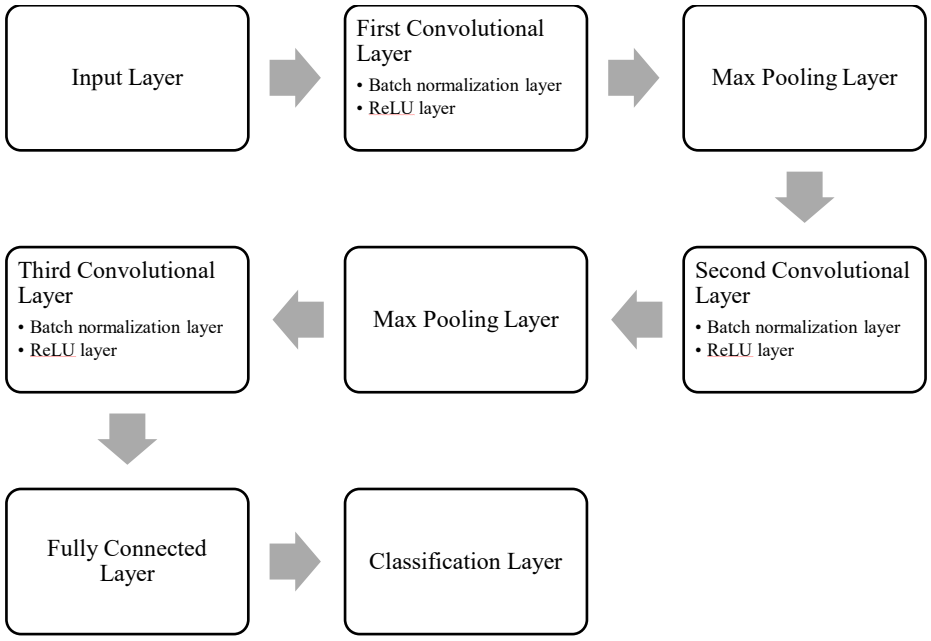

Figure 8. A diagram of the network architecture. Each convolutional layer had a 7 by 7 filter. The first convolutional layer had 8 filters, the second layer had 16 filters, and the third layer had 32 filters. Each max pooling layer has a 2 by 2 pooling region.

THIS PAGE INTENTIONALLY LEFT BLANK

V. CONVOLUTIONAL NEURAL NETWORK RESULTS

Figure 9 contains the confusion matrix of the neural network after validation, showing the number of cases classified correctly and incorrectly. The model performs at an overall 98% accuracy. The highest error occurs when distinguishing jet turbulence from wake turbulence. We have demonstrated that the spectra are similar between these cases, indicating that the dynamic processes are analogous, and this could explain the classification error between wake and jet turbulence. There are no instances of the network mistaking wakes and convection. Wakes, jet turbulence, and convective turbulence are classified correctly 91.5%, 97.3%, 99.6% of the time, respectively, demonstrating that wake turbulence is the most difficult to classify and that convection is structurally distinct from the other cases, making classification of convective turbulence easier. To gain a better understanding of which features are important for classification, we now observe the strongest activation channels for each layer and identify which features are commonly highlighted for each case.

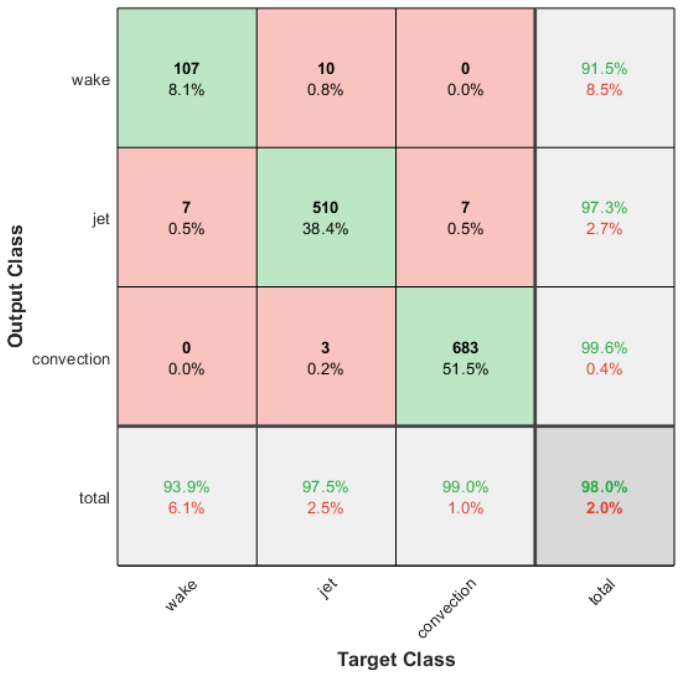

Figure 9. The classification confusion matrix. Red indicates an erroneous classification and green indicates correct classification.

We display the channel with the strongest activations for several examples in Figure 10 for the wake simulations, which can provide insight into important features discovered by each layer. Each layer consists of a set of two-dimensional arrays called channels. The number of channels for each layer is determined by the number of feature maps used. The feature maps operate on each channel of the previous layer. The input images are the same examples provided in Figure 7. We can observe from these examples that the first layer smooths the input image. The second layer appears to highlight regions where velocities increase in z. The third layer has strong activation channels for high gradients between small-scale features. This is the last convolutional layer before the fully connected layer, so the output analysis of this layer which focuses on high gradient small scale features is important for wake classification. This suggests the small-scale features in the near wake are important for detecting wakes.

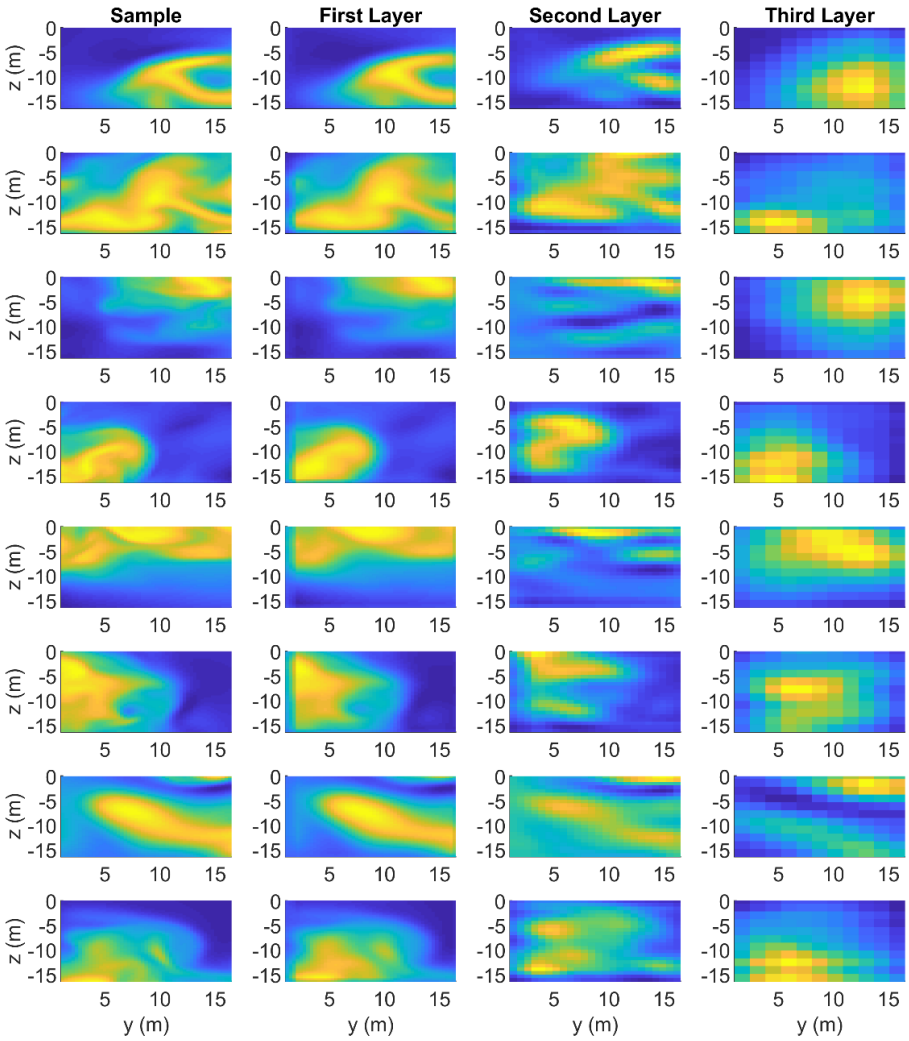

Figure 10. The strongest activation channels applied to the same wake samples in Figure 8. The original image is shown in the first column, then the strongest activation channels for the first, second, and third convolution layers proceed from left to right.

Figure 11 provides an example of the strongest activation channels of each convolutional layer in the network for the jet case. The convolutional layers behave similarly as for the wake case by initially smoothing the field and highlighting sharp gradients over small scales. This similarity could explain the network's confusion between the two flows. Even though there are similarities between wake and jet turbulence, we do observe that more features with weaker velocities are highlighted in the jet case when compared to the wake case. These weaker velocity features have large horizontal to vertical

aspect ratios, which suggests that turbulent jets create small-scale horizontal structures that may not be present in stratified wakes. To uncover important features of other turbulent sources, we turn now to convective turbulence as an example.

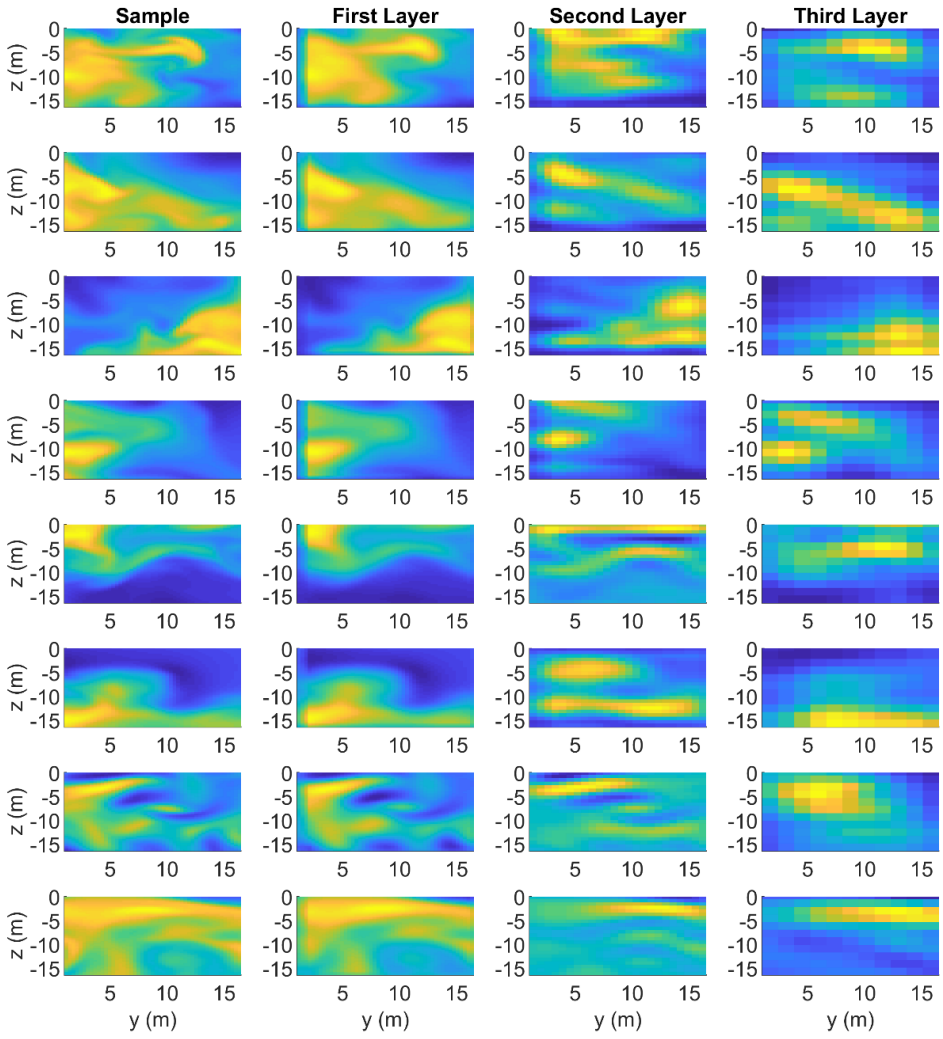

Figure 11. The strongest activation channels applied to the same jet samples in Figure 7, displayed in the same manner as Figure 10.

Figure 12 demonstrates the strongest activation channels for each convolutional layer of the convection samples provided in Figure 7. The convolutional layers highlight features in a similar way as in the other two cases, with the exception of the first layer,

which seems to invert some of the samples. The results show that the third convolutional layer has strong activations for areas with strong vertical gradients. In comparison to other sources of turbulence, horizontal features in convective turbulence do not appear as important to classification as is the case with turbulence generated by jets. In contrast with the wake case, the analysis of convective turbulence revealed that all strong vertical gradients are important, even those not associated with small-scale features.

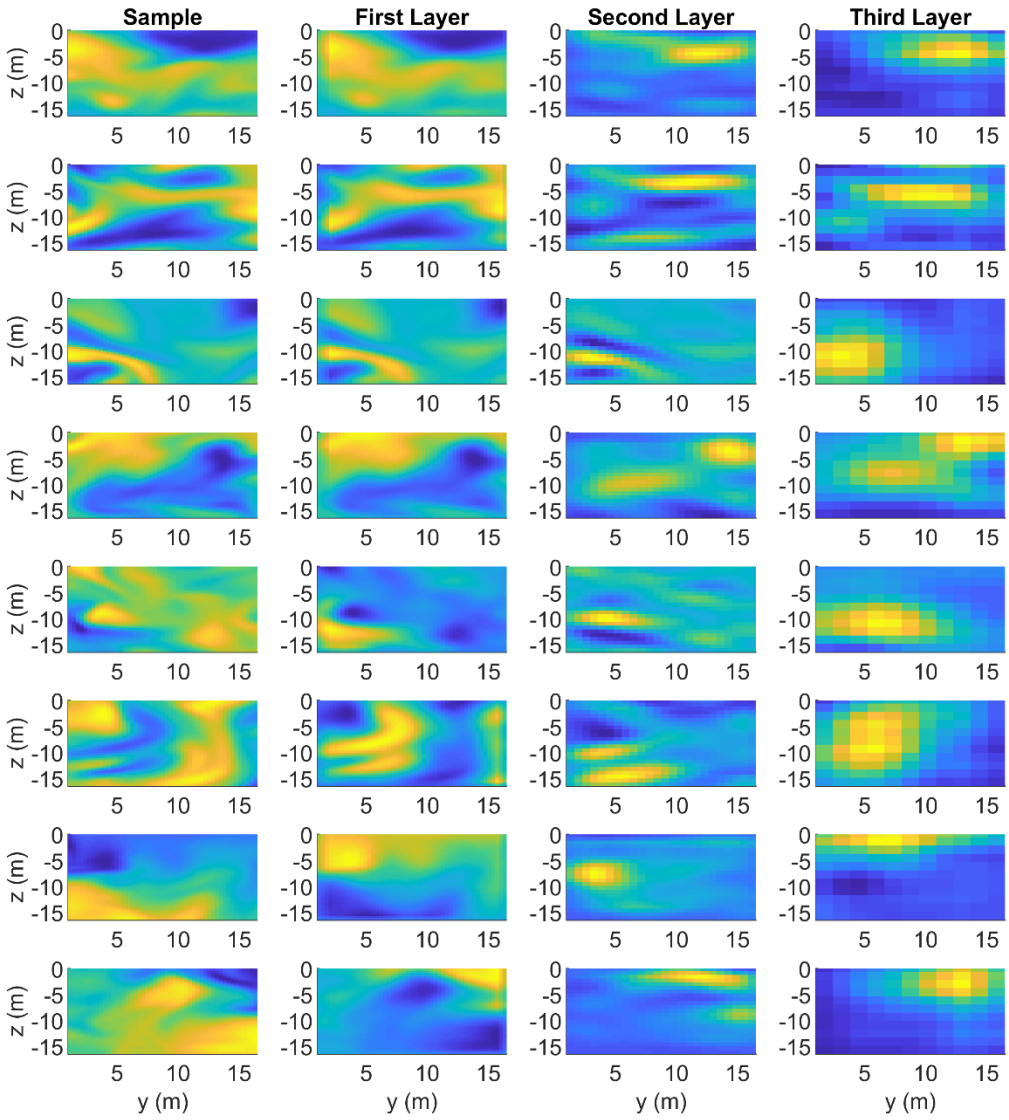

Figure 12. The strongest activation channels applied to the same convection samples in Figure 7 displayed in the same manner as in Figures 10 and 11.

THIS PAGE INTENTIONALLY LEFT BLANK

VI. DISCUSSION AND CONCLUSION

We have employed the Massachusetts Institute of Technology general circulation model to simulate wake turbulence and compared the results with turbulence generated by jets and convection. Visual comparison of the velocity field reveals that the turbulent flows between wakes, jets, and convection are similar, suggesting that wake detection from local measurements is difficult. The jet and wake spectra are similar except for smaller-scale features, which are more energetic in the jet case. These differences in the spectra suggest that small-scale turbulent features in the inertial range are important for classification. Given the differences of the spectra and the difficulty in visual classification, the identification of the wake and environmental turbulence is an ideal problem for artificial intelligence to solve.

The neural network described in this study classifies turbulent flows based on the velocity field at high accuracy. In the samples taken from each case, the neural network identifies small-scale features to classify the turbulence. The analysis of the jet case shows that horizontal features with high vertical gradients are important for classification. This suggests that turbulent jets produce small-scale horizontal features which are different from structures generated by other turbulent flows. The greatest source of the classification error is the difficulty in distinguishing the jet and wake turbulence. This confusion may be attributed in part to the similarities between the two spectra. Finally, the neural network assigns much weight in the convection classification to any region with high vertical gradients. This implies that both large and small structures are important features of convective turbulence. These results show that it is possible to identify turbulence solely based on high-resolution spatial data, which complements the work of Colvert et al. (2018), who showed that similar machine learning processes could classify turbulence based solely on time-series data. These two schemes could potentially be used in tandem to gather more information for characterizing wakes.

Demonstrating that turbulent structures are different among wakes, jets, and convection reveals that characteristics of turbulent structures may be dependent on the source that created them. Wind-generated shear flows or tides interacting with the seafloor

may have their own distinguishing characteristics. Ambient oceanic turbulence results from a wide range of processes which warrants further study to uncover unique structures produced by each process. Most importantly, data collected on these structures should be included in a neural network trained for wake detection. Any important features identified in these studies should be compiled into a dataset to provide diversity for future classification projects.

Since the power spectra of turbulent wakes, jets, and convection presented in this study show differences, a neural network has been shown to classify the source of turbulence based on two-dimensional spectra alone. Of interest is whether this method would improve the classification problem, particularly between wakes and turbulent jets. The spectra of these cases were similar visually, but any distinguishing characteristics uncovered through machine learning techniques and should be considered when assuming these flows are similar in future work.

More investigation is needed to determine if a neural network remains accurate in detecting intermediate and late wakes. Future studies that approximate stratified wakes with a jet should consider the differences between the flows uncovered by this study, particularly with small-scale features in the inertial range. For example, Diamessis et al. examined the power laws of an approximated isotropic wake using a jet with perturbations (2011), but we can see that the spectra for large wavenumbers in the inertial range have different power laws. More work is needed to understand the difference between turbulent jets and wakes to assess when approximating stratified wakes with turbulent jets is appropriate. In addition, our study is constrained to near wakes, so it would be valuable to investigate whether the neural network can detect salient features in late wakes because of their persistence. If successful, it may be possible to detect a wake at long time scales after the passage of a propagating submerged object.

The ability to detect a submarine using local velocity measurements relieves the reliance of the Navy on passive sonar for antisubmarine warfare. As adversarial submarines advance their noise-masking technologies, acoustic detection becomes increasingly difficult, requiring innovative alternatives for detection. More laboratory and field work is needed to improve the extant hydrodynamic detection algorithms. The experimental data

can be analyzed using neural networks to compare classification accuracy between numerical and lab experiments. It would be valuable to determine whether hydrodynamic detection is still possible in regions where the wake-induced and environmental turbulence are concurrently active. Finally, more field work on a submarine wake (e.g., Moody et al., 2017) is needed. Such efforts would provide definitive answers regarding the strengths, limitations, and prospects of submarine detection based on velocity field data collected in situ and processed using an artificial neural network.

THIS PAGE INTENTIONALLY LEFT BLANK

LIST OF REFERENCES

Afanasyev, Y. D., 2004: Wakes behind towed and self-propelled bodies: Asymptotic theory. *Physics of Fluids*, **16**, 3235–3238, https://doi.org/10.1063/1.1768071.

Anand, R. K., B. J. Boersma, and A. Agrawal, 2009: Detection of turbulent/non-turbulent interface for an axisymmetric turbulent jet: Evaluation of known criteria and proposal of a new criterion. *Exp Fluids*, **47**, 995, https://doi.org/10.1007/s00348-009-0695-5.

Balmforth, N. J., and Y.-N. Young, 2002: Stratified kolmogorov flow. *J. Fluid Mech.*, **450**, 131–167, https://doi.org/10.1017/S0022111002006371.

Bergé, P., and M. Dubois, 1984: Rayleigh-bénard convection. *Contemporary Physics*, **25**, 535–582, https://doi.org/10.1080/00107518408210730.

Bonneton, P., J. M. Chomaz, and E. J. Hopfinger, 1993: Internal waves produced by the turbulent wake of a sphere moving horizontally in a stratified fluid. *Journal of Fluid Mechanics*, **254**, 23–40, https://doi.org/10.1017/S0022112093002010.

Breda, M., and O. R. H. Buxton, 2019: Behaviour of small-scale turbulence in the turbulent/non-turbulent interface region of developing turbulent jets. *Journal of Fluid Mechanics*, **879**, 187–216, https://doi.org/10.1017/jfm.2019.676.

Colvert, B., M. Alsalman, and E. Kanso, 2018: Classifying vortex wakes using neural networks. *Bioinspir. Biomim.*, **13**, 025003, https://doi.org/10.1088/1748-3190/aaa787.

Chomaz, J. M., P. Bonneton, and E. J. Hopfinger, 1993: The structure of the near wake of a sphere moving horizontally in a stratified fluid. *Journal of Fluid Mechanics*, **254**, 1–21, https://doi.org/10.1017/S0022112093002009.

Chongsiripinyo, K., A. Pal, and S. Sarkar, 2017: On the vortex dynamics of flow past a sphere at Re = 3700 in a uniformly stratified fluid. *Physics of Fluids*, **29**, 020704, https://doi.org/10.1063/1.4974503.

Diamessis, P. J., J. A. Domaradzki, and J. S. Hesthaven, 2005: A spectral multidomain penalty method model for the simulation of high Reynolds number localized incompressible stratified turbulence. *Journal of Computational Physics*, **202**, 298–322, https://doi.org/10.1016/j.jcp.2004.07.007.

Diamessis, P. J., G. R. Spedding, and J. A. Domaradzki, 2011: Similarity scaling and vorticity structure in high-Reynolds-number stably stratified turbulent wakes. *Journal of Fluid Mechanics*, **671**, 52–95, https://doi.org/10.1017/S0022112010005549.

Dommermuth, D. G., J. W. Rottman, G. E. Innis, and E. A. Novikov, 2002: Numerical simulation of the wake of a towed sphere in a weakly stratified fluid. *Journal of Fluid Mechanics*, **473**, 83–101, https://doi.org/10.1017/S0022112002002276.

Garrett, C., and W. Munk, 1972: Space-Time scales of internal waves. *Geophysical Fluid Dynamics*, **3**, 225–264, https://doi.org/10.1080/03091927208236082.

Gourlay, M. J., S. C. Arendt, D. C. Fritts, and J. Werne, 2001: Numerical modeling of initially turbulent wakes with net momentum. *Physics of Fluids*, **13**, 3783–3802, https://doi.org/10.1063/1.1412246.

Guido Dehnhardt, Björn Mauck, Wolf Hanke, and Horst Bleckmann, 2001: Hydrodynamic trail-following in harbor seals (Phoca vitulina). *Science (American Association for the Advancement of Science)*, **293**, 102–104, https://doi.org/10.1126/science.1060514.

Hardisty, J., 2009: *The Analysis of Tidal Stream Power*. John Wiley & Sons, Incorporated.

Holliday, N. P., and J. F. Read, 1998: Surface oceanic fronts between Africa and Antarctica. *Deep Sea Research Part I: Oceanographic Research Papers*, **45**, 217–238, https://doi.org/10.1016/S0967-0637(97)00081-2.

Jiménez, J., A. A. Wray, P. G. Saffman, and R. S. Rogallo, 1993: The structure of intense vorticity in isotropic turbulence. *J. Fluid Mech.*, **255**, 65, https://doi.org/10.1017/S0022112093002393.

Lawrence, S., C. L. Giles, A. C. Tsoi, and A. D. Back, 1997: Face recognition: a convolutional neural-network approach. *IEEE Transactions on Neural Networks*, **8**, 98–113, https://doi.org/10.1109/72.554195.

Lewis, D. R., and T. Radko, 2020: On the structure and patterns of von Kármán vortices in two-dimensional high Reynolds number flows. *Physics of Fluids*, **32**, 116601, https://doi.org/10.1063/5.0022537.

Lin, Q., D. L. Boyer, and H. J. S. Fernando, 1992: Turbulent wakes of linearly stratified flow past a sphere. *Physics of Fluids A: Fluid Dynamics*, **4**, 1687–1696, https://doi.org/10.1063/1.858389.

Ling, J., A. Kurzawski, and J. Templeton, 2016: Reynolds averaged turbulence modelling using deep neural networks with embedded invariance. *J. Fluid Mech.*, **807**, 155–166, https://doi.org/10.1017/jfm.2016.615.

Marshall, J., A. Adcroft, C. Hill, L. Perelman, and C. Heisey, 1997: A finite-volume, incompressible Navier Stokes model for studies of the ocean on parallel computers. *Journal of Geophysical Research: Oceans*, **102**, 5753–5766, https://doi.org/10.1029/96JC02775.

The MathWorks, Inc, 2018: Deep Learning Toolbox™, R2018b.

Meunier, P., P. J. Diamessis, and G. R. Spedding, 2006: Self-preservation in stratified momentum wakes. *Physics of Fluids*, **18**, 106601, https://doi.org/10.1063/1.2361294.

Moody, Z. E., C. J. Merriam, T. Radko, and J. Joseph, 2017: On the structure and dynamics of stratified wakes generated by submerged propagating objects. *Journal of Operational Oceanography*, **10**, 191–204, https://doi.org/10.1080/1755876X.2017.1307801.

Poulin, F. J., and G. R. Flierl, 2003: The nonlinear evolution of barotropically unstable jets. *Journal of Physical Oceanography*, **33**, 2173–2192, https://doi.org/10.1175/1520-0485(2003)033<2173:TNEOBU>2.0.CO;2.

Radko, T., and D. Lewis, 2019: The age of a wake. *Physics of Fluids*, **31**, 076601, https://doi.org/10.1063/1.5100969.

Redford, J. A., T. S. Lund, and G. N. Coleman, 2015: A numerical study of a weakly stratified turbulent wake. *Journal of Fluid Mechanics*, **776**, 568–609, http://dx.doi.org/10.1017/jfm.2015.324.

Spedding, G. R., 1997: The evolution of initially turbulent bluff-body wakes at high internal Froude number. *Journal of Fluid Mechanics*, **337**, 283–301, https://doi.org/10.1017/S0022112096004557.

Spedding, F. K. Browand, and A. M. Fincham, 1996a: The long-time evolution of the initially turbulent wake of a sphere in a stable stratification. *Dynamics of Atmospheres and Oceans*, **23**, 171–182, https://doi.org/10.1016/0377-0265(95)00414-9.

Spedding, F. K. Browand, and A. M. Fincham, 1996b: Turbulence, similarity scaling and vortex geometry in the wake of a towed sphere in a stably stratified fluid. *Journal of Fluid Mechanics*, **314**, 53–103, https://doi.org/10.1017/S0022112096000237.

Spedding, G. R., 2014: Wake signature detection. *Annu. Rev. Fluid Mech.*, **46**, 273–302, https://doi.org/10.1146/annurev-fluid-011212-140747.

Theobald, O., 2017: Machine Learning for Absolute Beginners: A Plain English Introduction. Scatterplot Press.

Thorpe, S. A., 2007: *An Introduction to Ocean Turbulence*. Cambridge University Press.

Vaillant, R., C. Monrocq, and Y. L. Cun, 1994: Original approach for the localisation of objects in images. *IEE Proceedings - Vision, Image and Signal Processing*, **141**, 245–250, https://doi.org/10.1049/ip-vis:19941301.

Voropayev, S. I., G. B. McEachern, H. J. S. Fernando, and D. L. Boyer, 1999: Large vortex structures behind a maneuvering body in stratified fluids. *Physics of Fluids*, **11**, 1682–1684, https://doi.org/10.1063/1.870030.

Westerweel, J., C. Fukushima, J. M. Pedersen, and J. C. R. Hunt, 2009: Momentum and scalar transport at the turbulent/non-turbulent interface of a jet. *J. Fluid Mech.*, **631**, 199–230, https://doi.org/10.1017/S0022112009006600.

Yakovenko, S. N., T. G. Thomas, and I. P. Castro, 2011: A turbulent patch arising from a breaking internal wave. *J. Fluid Mech.*, **677**, 103–133, https://doi.org/10.1017/jfm.2011.64.

Zhang, Z. J., and K. Duraisamy, 2015: Machine learning methods for data-driven turbulence modeling. *22nd AIAA Computational Fluid Dynamics Conference*, 22nd AIAA Computational Fluid Dynamics Conference, Dallas, TX, American Institute of Aeronautics and Astronautics.

INITIAL DISTRIBUTION LIST

1. Defense Technical Information Center
   Ft. Belvoir, Virginia

2. Dudley Knox Library
   Naval Postgraduate School
   Monterey, California